Structure of amorphous TeO 2 revisited: A hybrid functional ab initio molecular dynamics study

Raghvender Raghvender, Assil Bouzid, Sylvian Cadars, David Hamani, Philippe Thomas, Olivier Masson

The structure of amorphous TeO_2 revisited: A hybrid functional *ab-initio* molecular dynamics study

Raghvender Raghvender, Assil Bouzid,* Sylvian Cadars, David Hamani, Philippe Thomas, and Olivier Masson
Institut de Recherche sur les Céramiques (IRCER), UMR CNRS 7315-Université de Limoges, France.
(Dated: October 25, 2022)

The atomic-scale structure of glassy TeO_2 has been the subject of a longstanding debate. We resort to first-principles molecular dynamics with a careful choice of the exchange and correlation functional to achieve a good agreement with experimental findings for the topology of glassy and molten TeO_2. We show that only molecular dynamics at the hybrid functional level of theory is able to reproduce a correct description of the medium range order in the glass. Based on a Wannier-function decomposition of the electronic structure we show that the coordination number of tellurium is around 4 and that there is a non negligible fraction of non-bridging oxygen atoms. An analysis of the net atomic charge distribution shows that an increase of the Te-O-Te bridge asymmetry strongly correlates with the charge on the oxygen atom. Additionally, we find that the oxygen bridge asymmetry increases with temperature, which strengthen the short-range disorder in molten TeO_2, and consequently lower the coordination number of Te. These results provide a revisited picture of the TeO_2 network connectivity and its evolution as a function of temperature.

I. INTRODUCTION

Tellurite glasses are frequently studied due to their distinctive physical properties, which include a high refractive index, good non-linear optical properties, high dielectric constant, low phonon energies, high chemical stability, low melting temperatures, large thermo-optical coefficient and wide optical transmittance in the visible to near-infrared region[1–6], allowing them to be used in a wide range of applications. These distinguishing characteristics make them suitable for usage as optical switching devices[7], erasable optical recording media[8], optical amplifiers, up-conversion frequency systems and laser hosts[5,9]. Remarkably, TeO_2-based glasses feature a high non-linear optical susceptibility among other oxide glasses[10], attracting therefore a considerable interest to this family of compounds. The origin of these properties has been early attributed to the electronic ($5s^2$) lone pair of tellurium (IV) atoms when bonded to oxygen atoms[11]. Recent works suggest that the structure of the glass itself and in particular the nature of the Te-O-Te bridges[12–14] is responsible to a large extent for these properties. Despite its wide technological relevance, the atomic-scale description of TeO_2 glass remains elusive and no general consensus has been so far established.

Tellurium dioxide TeO_2 can be found in several polymorphs, including α-TeO_2, β-TeO_2, γ-TeO_2, and δ-TeO_2[15–19]. The α-TeO_2 variety (paratellurite) is stable at ambient pressure whereas the β-TeO_2 phase (the natural form of the tellurium dioxide) is metastable and transforms irreversibly to the paratellurite at 600°C. The γ- and δ-polymorphs are obtained during crystallisation of TeO_2-rich glasses. They both transform irreversibly to α-TeO_2 at temperature above 450°C. The structures of these polymorphs are all characterised by the presence of stereochemically active lone pair of tellurium (IV) atoms, which produces a strong asymmetry in the oxygen atom environments. The main structural units are TeO_4 disphenoids with two short equatorial Te-O bonds and two longer axial bonds. In α-TeO_2, the disphenoids are connected *via* single Te-O-Te bridges and form a three-dimensional network, whereas in β-TeO_2, the tellurium atoms are connected *via* double bridges, forming a layered network. The γ-TeO_2 consists of corner sharing TeO_{3+1} units, where one $Te-O$ bond is substantially larger than the other three and appears as a chain-like structure when these longer bonds are disregarded. As a result, γ-TeO_2 can be classified as a polymeric TeO_3-based form of TeO_2. The δ-TeO_2 polymorph has a fluorite-type average structure with a very high positional disorder, especially for oxygen. It is best described as an intermediate state between the amorphous and crystalline states. Interestingly, α-TeO_2 and γ-TeO_2 have shown ~ 40 and ~ 30 times higher third order non-linear susceptibility, respectively, as compared to structurally similar α-SiO_2[20].

During the last two decades, various approaches such as neutron diffraction[21], Raman spectroscopy[21,22], magic angle spinning (MAS)-nuclear magnetic resonance (NMR)[23,24], neutron and total X-ray diffraction combined with reverse Monte Carlo (RMC) simulations[25–28] have been used to investigate the structure of modified TeO_2-based glasses. The overall picture stemming from these studies describes TeO_2 glass as a complex system made up of several TeO_x structural units with either bridging oxygen (BO) or non-bridging oxygen (NBO) atoms, the amount of the latter increasing with the modifier content. These units are usually referred to as Q^n_m units, where m denotes the total number of bonding oxygen and n denotes the number of BO atoms.

In the case of the pure TeO_2 glass, the presence of NBO atoms, or terminal Te=O groups, is much less clear. In particular, the exact value of the average coordination number of Tellurium atoms (n_{TeO}), indicative of the presence of terminal oxygen atoms (if less than four), remains a matter of debate in the community. In the work by Barney et al.[21], neutron diffraction and Raman spectroscopy measurements of the structure of pure TeO_2 revealed that the glass is made of two-third four coordinated (trigonal bipyramid) and one-third three coordinated (trigonal pyramid) tellurium units. On the contrary, solid-state NMR in conjunction with first-principles calculations, Raman spectroscopy and total X-ray diffraction revealed the lack of three-fold coordinated Te in TeO_2 glass[22]. In this work, the authors used a topology constraint model to refute the prior assertions by Barney's earlier statements[21]. In their model, Garaga et al. reported a Te coordination number around 3.75, which is slightly higher than what was predicted in the studies by Gulenko et. al.[29] (n_{TeO}=3.63) and by

Pietrucci et. al.[30] (n_{TeO}=3.69). As a result, the authors dismiss the presence of terminal oxygen, claiming that considering three-fold coordinated tellurium units in the description of the network oversimplifies this issue. In a further NMR spectroscopy study by Marple et al.[31], the authors reveals the presence of 89% of TeO_4 units along with 11% of TeO_3 units in TeO_2 glass which results in a Te coordination number of 3.9, slightly higher than the one reported by Barney et al.[21]

In a recent work by Alderman et al.[32], the authors used high-energy X-ray diffraction as this technique is less sensitive to O-O interactions and more sensitive to Te-O interactions in TeO_2 glass compared to neutron diffraction, allowing consequently to have a better access to the Te coordination number. The authors reported the presence of Q_4^4 units (coordination number ≈ 4) with a wide distribution of asymmetric Te-O-Te bridges. In addition, due to the presence of highly asymmetric Te-O bonds, no apparent distance cut-off between bonded and non-bonded Te-O was possible to establish at high temperatures (melt state). The long and weak Te-O bonds undergo larger anharmonicity as a result of the strong temperature fluctuations, which makes the long Te-O bond to be no longer qualified as a bonded interaction after a certain point, causing a compensation through the contraction of the short bonds in the Te-O-Te bridge. Ultimately, this leads to a reduction of the coordination number in molten TeO_2 compared to the glass. The investigation of the pair distribution functions (PDF) in their work supports this finding, revealing a slightly shorter Te-O bond distance of 1.919 Å in the melt compared to 1.926 Å in the glass.

On the computational side, an *ab-initio* study[30] of a model of 32 TeO_2 units corresponding to a density of 5.84 g/cm^3 with Becke-Lee-Yang-Parr (BLYP) functional reported the coordination number of glassy TeO_2 to be 3.69 (defined with a Te-O cut-off radius of 2.36 Å). Moreover, classical molecular dynamics (CMD) studies by Gulenko et. al.[29] revealed n_{TeO} to be 3.63 with a Te-O cut-off radius = 2.46 Å. Both investigations reveal that the evolution of the coordination number as a function of Te-O cut-off radius increases continuously without any flat plateau, which indicates the presence of considerable range of Te-O distances in glassy TeO_2 network. This brings the problem in establishing a clear cut-off radius value for defining Te atom's first coordination sphere[30,33], and more fundamentally it raises the question whether a clear separation between three- and four-coordinated Te atoms can be made given the high versatility of this element in TeO_2 melts and glasses. The Q_m^n structural units distribution found in both mentioned *ab-initio* and CMD studies are quite similar. Additionally, Torzuoli et al.[34] proposed a refined version of the Te-O interatomic potential and reported the occurrence of 21% NBO which is 7% larger than the one reported by Pietrucci et al.[30].

Despite the success of the aforementioned works in elucidating the structure of TeO_2 glass and its related properties they suffer from several limitations. On the one hand, *ab-initio* modeling[30] was performed on a small system size and during a short simulation time, which may lead to nonphysical constraints in the system. On the other hand, classical interatomic potentials rely on an empirical formulation of the various interactions between the particles and is fitted on either experimental or high-level theoretical data. Hence, this approach highly depends on both the empirical formulation of the interaction potential, and on the data on which it was fitted. Consequently, this method leads generally to a less accurate structural description of the studied system. Overall, because of these limitations, none of the various and sometimes contradictory models proposed in the literature provides a complete and comprehensive description of the structure of TeO_2 glass, which remains elusive despite its chemical simplicity.

In the present work, we push further our understanding of the structure of TeO_2 systems by relying on various molecular dynamics (MD) simulation techniques based on density functional theory (DFT). First, we focus on establishing a modeling scheme able to reproduce the main structural features of glassy and molten TeO_2 measured experimentally from total X-ray scattering with a particular focus on the use of hybrid exchange and correlation functional. Then, we develop a scheme that allows one to define the coordination number of tellurium with less ambiguity and study the network connectivity and the short range order evolution as a function of temperature. Finally, we focus on the short range disorder around Te and O atoms in relation to the chemical environment and net atomic charge distribution between neighbors in both molten and glassy TeO_2. Our results provide a revisited view of the atomic-scale structure of TeO_2 system in agreement with recent experimental data.

The paper is organized as follows. Computational details are presented in section II where the various molecular dynamics schemes are illustrated in subsection II A and the TeO_2 model generation and validation processes are presented in subsection II B. Results, including the pair distribution functions, coordination numbers, short range disorder and atomic local environments, charge analysis and electron localization are presented in section III. The conclusions of our work are drawn in section IV.

II. COMPUTATIONAL DETAILS

A. First-principles molecular dynamics simulations

In this work, we resort to first-principles molecular dynamics (FPMD) to produce amorphous and melt models of TeO_2. In particular, several molecular dynamics schemes were employed depending on the simulation length and DFT setup. In what follows, we briefly outline the methodology behind each MD scheme.

1. Car-Parrinello molecular dynamics

The electronic structure is described within the Density Functional Theory where electron exchange and correlation energy was described through generalized gradient approximation (GGA). In particular, we resort to two GGA functionals, namely the Perdew-Burke-Ernzerhof (PBE) functional[35]

and the BLYP functional[36,37]. Valence electrons are treated explicitly and represented by a plane-wave basis set expanded at the point of the simulation cell with an energy cutoff of 80 Ry. The valence-core interactions are described by norm-conserving pseudopotentials of the Troullier-Martins type[38]. Molecular dynamics within the scheme of Car-Parrinello (CPMD)[39] are carried out as implemented in the CPMD computer code[40]. A fictitious electron mass of 500 a.u. and a time step of t = 0.12 fs is used to integrate the equations of motion, ensuring good control of the conserved quantities. The temperature for both the ionic and electronic degrees of freedom is controlled by a Nosé-Hoover thermostat[41–43].

2. Born-Oppenheimer molecular dynamics

The electronic structure calculations are performed with the CP2K code,[44] which is based on the Gaussian Plane Waves (GPW) method to solve the Kohn-Sham equations. Within this method, the orbitals are described with an atom-centered Gaussian-type basis set of type triple-ζ[45], and the electron density is expanded on an auxiliary plane-wave basis set. The plane-wave energy cutoff is set to 500 Ry and the Brillouin zone is sampled at the Γ point. Goedecker-Teter-Hutter pseudopotentials are used to describe core-valence interactions.[46] We use either GGA (PBE or BLYP) or PBE0 hybrid functional to calculate the DFT energy,[47,48]. Molecular dynamics simulations are carried out within the Born-Oppenheimer (BOMD) framework with a time step of t = 1 fs and a Nosé-Hoover thermostat[41–43] to ensure the temperature control.

3. Second generation Car-Parrinello molecular dynamics

In order to reach long time scales at affordable computational cost, we resort to the Second Generation Car-Parrinello molecular dynamics due to Kühne et al.[49] implemented in the CP2K suite of programs. In this scheme, the wavefunctions are not self-consistently optimized during the dynamics in analogy to the Car-Parrinello MD, while large integration time steps typical of Born-Oppenheimer MD can be used. This scheme leads to a slightly Langevin-type dissipative dynamics governed by the following equation:

$$M_I\ddot{R}_I = F_{BO} - (\gamma_D + \gamma_L)\dot{R}_I + \Xi_I \qquad (1)$$

where M_I, R_I and F_{BO} are the particle mass, the ionic coordinates and the the Born-Oppenheimer forces, respectively. γ_D, γ_L and Ξ_I are the intrinsic and Langevin friction coefficients and a random noise term. Although dissipative, an accurate sampling of the Boltzmann distribution can be achieved by an appropriate choice of the friction coefficients such that the noise has to obey the fluctuation-dissipation theorem[49]: $< \Xi(0)\Xi(t) >= 6(\gamma_D + \gamma_L)M_I k_B T\,\delta(t)$. In the case of TeO_2, we used the same DFT setup as for BOMD in section II A 2. In addition, the values of γ_D and γ_L were fixed to 0.0005 fs^{-1} and 0.1 fs^{-1} for temperatures ranging from 1000 K to 500 K and to 0.0007 fs^{-1} and 0.1 fs^{-1} for temperatures below 500 K, respectively.

B. TeO_2 Model generation

In this work, seven TeO_2 glassy models were generated by quenching from the melt. In particular, we have produced five models at the GGA level of theory: a 270 atoms model using CPMD and PBE functional at the experimental density of 5.57 g cm^{-3} (Model S1), Model S2 in similar fashion to Model S1 except the use of BLYP functional, Model S3 is similar to model S2 but contains 480 atoms, Model S4 is similar to model S3 but was produced through BOMD, Models S5 resorts to the SGCPMD at the PBE level of theory with 270 atoms over a long quenching period. Furthermore, two models at the hybrid functional level of theory were produced using BOMD, PBE0 functional, 270 atoms at the experimental density (Model 1), and with a variable density scheme (Model 2). All the details related to these models are provided in the supplementary materials[50] (see, also, references [29,32,51,52] therein). These models allow to evaluate the effects of the adopted DFT setup (model S1 vs. model S2 and models S1, S2 vs. models 1, 2), size of the model (models S1, S2, S3 vs. model S4) and quenching protocol (model S1 vs. S5) on the final structure of the glassy system compared to experimental measurements. A detailed comparison of the various models is provided in the supplementary materials[50].

This set of models allowed us to asses the best modelling strategy to achieve an accurate atomic scale model of glassy TeO_2. To this end, the quality of the model is first evaluated by comparing the calculated X-ray total pair correlation function to experimental measurements in the molten and glassy states[32] of TeO_2. PDFs allow a direct access to the structure of the glassy and molten material and could be directly compared to experiments. Although there are available NMR and Raman spectroscopy measurements for glassy TeO_2, their computational counterpart remains challenging to achieve on a large periodic systems at the DFT level of theory. In addition, the interpretation of NMR and Raman data remains difficult due to the broad spectra usually obtained. As such, we focus on the PDF as a tool to validate our models in comparison to experiments. In addition, we compare the calculated total X-ray structure factor to experiments when needed.

The total pair distribution function (PDF) $G(r)$ is usually calculated by combining the partial pair correlation functions $g_{\alpha\beta}(r)$ as follows:

$$G(r) \approx \sum_{\alpha=1}^{2}\sum_{\beta=1}^{2} \frac{c_\alpha c_\beta f_\alpha(k_0) f_\beta(k_0)}{|\langle f(k_0)\rangle^2|}\left[g_{\alpha\beta}(r) - 1\right]. \qquad (2)$$

where α and β refer to one of the involved chemical species (Te and/or O). c_α and $f_\alpha(k)$ are the atomic concentrations of species α (Te, or O) and its corresponding scattering factor. In this formulation, the scattering factors are usually taken at a $k_0 = 0$, which often leads to an overall good representation of $G(r)$ but with an ill description of the magnitude of the first peaks of the PDF. In order to go beyond this limitation, we here use the exact $G(r)$ expression from Ref. [53] where, $G(r)$ can be obtained through a weighted linear combination of modified partial pair correlation functions. The weights

are defined as the mean values of the Faber−Ziman factors over the considered reciprocal space range. The calculated PDFs on all our GGA models are presented in Fig. S1 in the supplementary materials[50].

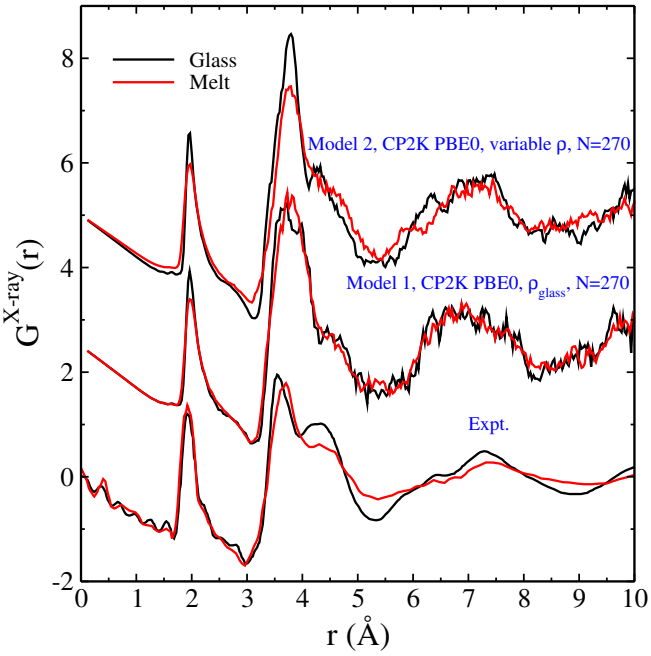

FIG. 1. Total PDF computed for amorphous (black lines) and melt (red lines) TeO_2 obtained from Models 1 and 2 compared to experimental results from Ref. [32]. The curves are shifted vertically for clarity.

Careful examination of all models derived from setups utilizing the GGA level of theory (see supplementary materials[50]) establishes that the observed similarities between PDFs of molten and glassy TeO_2 neither depend on the model characteristics (size and XC functional) nor on its thermal history (see Fig. S1 in the supplementary materials[50]) but are more probably related to an inadequate level of theory. Indeed, as the particular geometry of the TeO_x structural units depends on the position of the electronic lone pair, which itself depends on the electronic localisation level, the ability of the chosen level of theory to precisely describe electronic localization is expected to impact the quality of the models. However, the GGA level of theory is known to promote electronic delocalization and therefore may be insufficient to achieve a correct description of the TeO_2 systems. In order to verify this hypothesis, we have produced a model by resorting to hybrid XC functional (Model 1). In particular, the PBE0 hybrid functional comprising a fraction of 25% of Hartree-Fock exchange, is expected to lead to a better description of the electronic structure of oxide materials which in turn leads to an improved local structures compared to those produced in otherwise similar conditions at the GGA level of theory[54–58]. Nevertheless, the prohibitive computational cost of such a hybrid functional molecular dynamics (more than 10 million core hours for the present work) prevents the production of extended trajectories. In order to have a significant melt-like diffusion at high temperature, we annealed the Model 1 at T=1200 K, a temperature slightly higher than the melting point (T=1006 K) before quenching to T=300 K (details of the model production are available in the supplementary materials[50]). The obtained PDFs for glassy and molten TeO_2 (Model 1) are presented in Figure 1.

We observe the presence of a shoulder in the PDF of the glass at around 4.5 Å, close to the position of the measured third peak around 4.3 Å. Nevertheless, this shoulder remains almost the same as a function of the system temperature. Overall, the calculated PDFs show small differences between molten and glassy TeO_2. While these findings show that a better description of the electron localization (see Fig. S3 in the supplementary materials[50]) induces an impact on the structural organization of the disordered system compared to GGA functionals, a better reproduction of the third peak intensity requires additional efforts. In particular, this peak assigned to neighboring Te atoms, might be affected by the fixed volume of the cell during the melt-quench cycle. To cope with this issue, we repeated the thermal cycle of Model 1, to produce a new system (Model 2) where the density was linearly reduced from the melt density (at $T \geq 1000$ K) to the glass density (details of the model production are available in the supplementary materials[50]). We note that this approach is similar to molecular dynamics in the isobaric isothermal ensemble (NPT). While the NPT approach requires very extended molecular dynamics runs in order to ensure the convergence of the cell volume, in the constant density approach the volume is fixed and fitted to the experimental reference densities. This approach ensures structural relaxation at various densities and temperatures mimicking the experimentally observed density variations.

The computed PDFs at PBE0 XC functional and variable density (Model 2) are presented in Figure 1. We observe that the overall shape of the PDFs is enhanced comparing to that of Model 1. The PDFs of molten and glassy TeO_2 now show differences in shape and position of peaks that are remindful of those present in the PDFs measured experimentally. In particular, the shift and change of the shape of the shoulder visible between molten and glassy TeO_2 are consistent with experiment. Specifically, we distinguish a peak at around 4.3 Å in the PDF of the glassy TeO_2 similar to that observed experimentally. This peak is better reproduced than with any of the previous models and its origins will be discussed in section III A. We note that, although the second peak in the PDF does not perfectly reproduce the experimentally observed peaks in the glassy and molten TeO_2 and that its intensity is slightly overestimated, it reflects a structural change in the network connectivity upon cooling as measured experimentally. As for the minima observed in the calculated PDFs at 3 and 5.3 Å, they fairly reproduce the experimental measurements as this latter shows a strong error bar due to the uncertainty on the melt density[32]. Overall, Model 2 appears to better capture the structural changes occurring as the system is quenched to room temperature.

For completeness, we carried out the same variable-density

melt quench as used for Model 2 at the PBE level of theory (data not shown). The obtained model was found to be very similar to Model S1 (see supplementary material[50]) which supports the role played by the improved electronic description of the hybrid functional to obtain a correct description of glassy and molten local structures of TeO_2.

In order to consolidate the TeO_2 structure obtained from Model 2, we present in Fig. 2 the X-ray total structure factor $S(Q)$ obtained by Fourier transform of the total PDF and compare it to experimental results. We find a good agreement between the measured and the computed $S(Q)$ over all the reciprocal space region. In particular, our model reproduces the shift in the position of the first diffraction peak to larger Q values and the increase of its intensity as measured experimentally when the temperature is reduced[32].

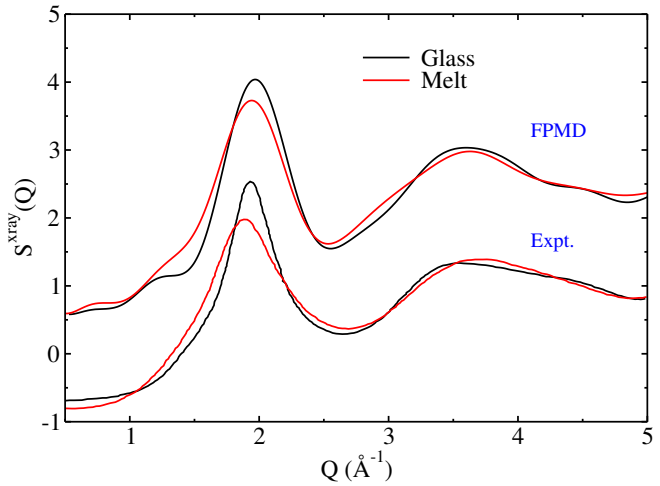

FIG. 2. Total X-ray structure factor computed for amorphous (black lines) and melt (red lines) TeO_2 compared to experimental results from Ref. [32].

All these results suggest that a good modelling of molten and glassy TeO_2 requires the combination of two important ingredients: an accurate description of the electronic structure through the use of hybrid XC correlation functionals, and a proper account of the system density during the glass production process. Although there certainly remains room, on paper, to further improve the amorphous TeO_2 models presented here through extended FPMD (larger model sizes, multiple initial states, longer quenching rates and averaging over multiple trajectories) at the hybrid functional level of theory, in practice their cost is presently prohibitive. To achieve such goals one will have to resort to different strategies, such as machine learning atomic interaction potentials trained based on DFT calculations at the hybrid level of theory (including those presented here), but this is well beyond the scope of this work. Here, in light of all the concordant elements discussed above, one can rely on Model 2 to investigate the atomic scale structure of glassy and molten TeO_2 with an unprecedented level of accuracy and reliability. This is the focus of the next section.

III. RESULTS

A. Partial pair distribution functions

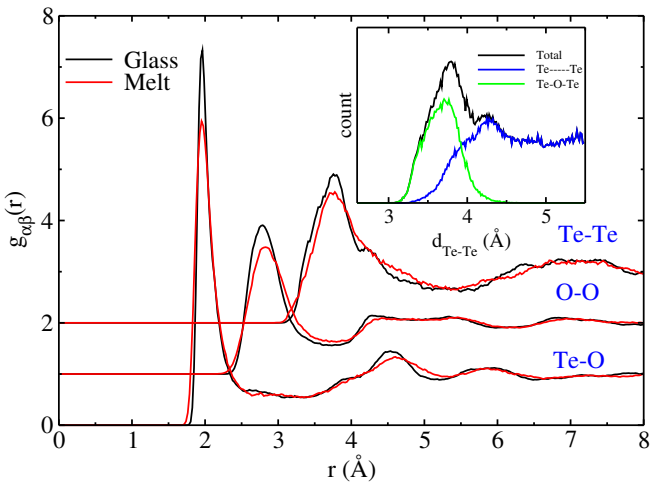

FIG. 3. The partial pair correlation functions $g_{TeTe}(r)$, $g_{TeO}(r)$, and $g_{OO}(r)$ for amorphous (black lines) and melt (red lines) TeO_2. The curves are shifted vertically for clarity. The inset shows the break down of the Te-Te distance distribution into contributions from Te atoms connected through at least one O bridge (green color), and neighboring Te atoms not directly sharing any O (blue color).

A first insight into the atomic scale structure of the amorphous TeO_2 system is obtained by looking at the partial pair distribution functions ($g_{\alpha\beta}(r)$) of Model 2 presented in Fig. 3. The first peak in the Te-O PDF corresponds to the first peak of the total PDF shown in Fig. 1. We remark that the position of this peak moves from 1.964 Å in the glass to 1.952 Å in the melt. These results are in agreement with their experimental counterpart where the same first peak has been observed to move from 1.926 Å in the glass to 1.919 Å in the melt. The slight overestimation (≈0.03-0.04 Å) of the Te-O bond length in our models is mainly due to the adopted DFT setup[30,59]. Coming to the first peak of the O-O PDF, it only appears for distances larger than 2.3 Å in agreement with X-ray diffraction results[32] and does not show a significant contribution to the total PDF due to the small scattering factor of O atom [$f_O(k_0{=}0) \approx Z_O = 8$] as compared to Te atom [$f_{Te}(k_0{=}0) \approx Z_{Te} = 52$]. Nevertheless, this peak position exhibits a shift from 2.79 Å to 2.83 Å as the temperature increases. These changes in the Te-O and O-O correlations reflect the significant alteration of the local environment around Te, and consequently the alteration of short range order as a function of temperature. These findings are also reflected in the Te-Te PDF, where beside a barely visible displacement of the Te-Te main peak position towards smaller distances, a shoulder appears around 4.25 Å when the system is quenched to room temperature. We note that the choosen DFT setup might impact the shoulder position and shape. The aforementioned two features can be respectively attributed to Te atoms connected through at least one O bridge (Te-O-Te), and neighboring Te atoms not

directly sharing any O (see inset of Fig. 3). The absence of the Te-Te shoulder around 4.25 Å in the melt suggests that not only the short range order is affected at high temperature, but also the medium range organisation of Te atoms.

B. Coordination numbers and atomic local environments

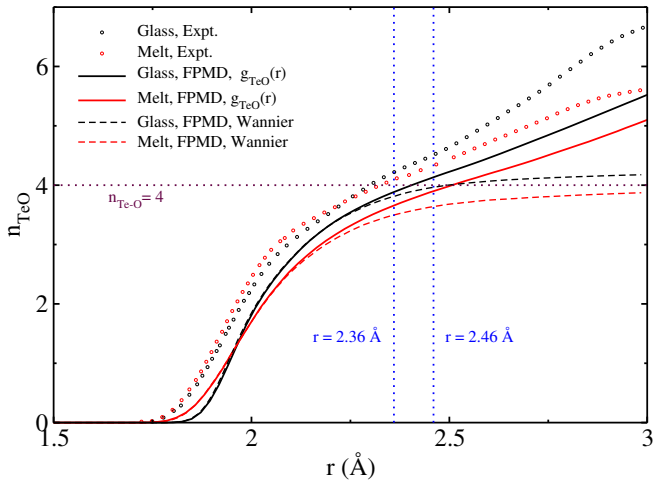

FIG. 4. Running Te-O coordination number ($n_{TeO}(r)$) of amorphous (black color) and melt (red color) TeO_2. Results obtained by integration of the Te-O partial PDF (solid lines) and based on Wannier centers (dashed lines) are compared to experimental results (circles) from Ref. [32]. Vertical dashed lines indicate distance cutoffs and the dashed horizontal line indicates the ideal Te^{4+} coordination number.

More insights into the local environment can be obtained by calculating the integral of the partial pair distribution functions. This quantity, $n_{\alpha\beta}(r)$, corresponds to the coordination number of a given chemical species α with respect to species β. Fig. 4 shows the evolution of the running Te coordination number n_{TeO} calculated on molten and glassy TeO_2 as a function of the Te-O distance and compared to their experimental counter part[32]. We remark that the calculated coordination numbers are slightly displaced towards the large r values compared to experiments. This shift of about 0.05 Å is due the displacement of the calculated first peak of the Te-O PDF compared to the measured one. The same shift is also visible in the total PDF (see Fig. 1). In spite of this shift, we find that the calculated n_{TeO} follows closely the pattern measured experimentally, showing a continuous increase over all the r range, which reflects the absence of a clear first minimum in the Te-O PDF. In addition, our models reproduce the smaller Te coordination number found in the melt compared to the glass. This reduction was attributed in previous studies to the increase of the short range disorder around Te atom[32]. In particular, at high temperatures Te looses some long and weak bonds with O atoms leading to a reduction of the coordination number[32,60]. We recall that the short range disorder is the result of the deviation from the ideal local structural arrangements that are generally found in the crystalline structures.[61]

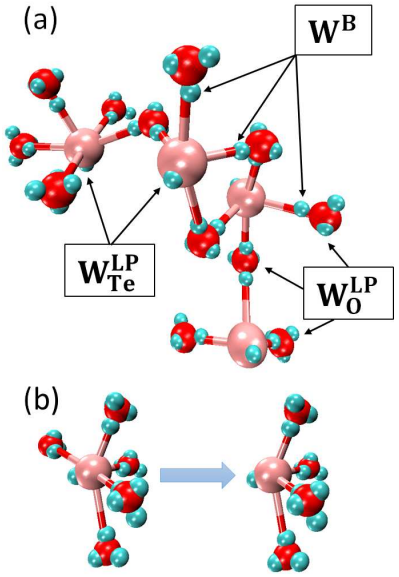

FIG. 5. (a) A representative snapshot of bonding environment in glassy TeO_2. Te (brown), O (red), and Wannier centers (labeled as W) (cyan). Only a few Te and O atoms are presented along with representative Wannier centers. We distinguish three different Wannier centers: W_B centers occurring along Te-O bonds, W^{LP}_{Te} and W^{LP}_{O} indicate the lone pair (LP) valence electrons not participating in chemical bonds. (b) A representative Te environment where the O neighbors are identified based on a fixed cutoff distance (left image) and based on MLWF constraints (right image).

By inspecting Fig. 4, an unambiguous estimation of the Te coordination number is not straightforward as one cannot clearly define a Te-O distance cutoff due to the ill definition of the Te-O PDF first minimum. This results in the absence of a plateau in the $n_{TeO}(r)$ that could be used to uniquely determine the average coordination number. In literature, an arbitrary cutoff of 2.36 to 2.46 Å was often used to estimate the Te coordination number[29,30,32,59]. In this work, we use instead the maximally localized Wannier functions (MLWF)[62,63] in order to improve the accuracy of the determination of the network connectivity. Within this scheme, a Wannier function ($w_n(\mathbf{r})$) corresponds to the localization of two electrons and its center (W) gives its average position. $w_n(\mathbf{r})$ are obtained by an on the fly unitary transformation of the Kohn-Sham orbitals $\psi_i(\mathbf{r})$ under the constraint of minimizing the spatial extension (spread, Ω) of the resulting $w_n(\mathbf{r})$ as follows:

$$\Omega = \sum_n \left(\langle w_n | \mathbf{r}^2 | w_n \rangle - \langle w_n | \mathbf{r} | w_n \rangle^2 \right) \tag{3}$$

Hence, MLWF leads to an accurate and compact real-space representation of the electronic structure, which can be used to define chemical bonds and lone pair electrons. Wannier functions were computed on top of 100 configurations selected along the trajectory at T = 300K. Figure 5(a) shows a representative fragment of TeO_2 glass, where we distinguish three

types of Wannier centers. W^B refers to centers occurring at a Te-O bond, W^{LP}_{Te} and W^{LP}_{O} refer to centers representative of lone-pair electrons at the vicinity of Te and O atoms, respectively.

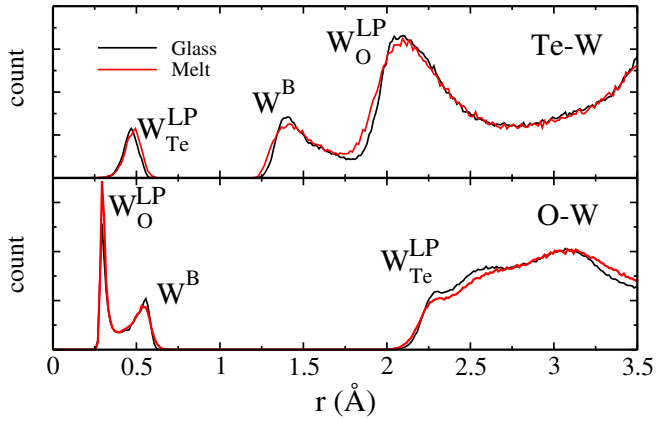

FIG. 6. Distribution of the Wannier centers around Te (top panel) and O (bottom panel) in amorphous (black lines) and melt (red lines) TeO_2.

Fig. 6 shows the distribution of Wannier centers around Te and O in molten and glassy TeO_2 where we distinguish three main peaks. The first peak is attributed to W^{LP} at the vicinity of a chosen atom, the second peak is due to bonding Wannier W^B, and the last peak is attributed to W^{LP} occurring at the first neighboring atoms. In contrast to the $g_{TeO}(r)$, a Te-O cutoff distance can be defined from the positions of the Te-W^B and O-W^B second minimum positions in Fig. 6. These distances correspond to the farthest position of a shared Wannier center occurring along the Te-O bond and when summed up provide a reasonable estimation of the Te-O cutoff. Based on this assumption we find that Te-O cutoff distances are 2.46 Å and 2.47 Å in glassy and molten TeO_2, respectively. We remark that this cutoff is 0.1 Å larger than the 2.36 Å usually reported in the literature. This small difference is attributed, on the one hand, to the small overestimation of Te-O bonds in our model ($\approx$ 0.05 Å), and on the other hand, to statistical error due to Wannier centers occurring slightly off the Te-O bond which usually leads to a deviation smaller than 0.05 Å in the estimated Te-O distance. By integration of the partial Te-O PDF up to the obtained cutoff distances, we find a Te coordination number n_{Te} of 4.12 and 3.91 for glassy and molten TeO_2, respectively. These results are in agreement with those obtained from experiments based on a cutoff of 2.36 Å: 4.22 and 4.09 for glassy and molten TeO_2[32], respectively. Hence, these results reveal that the coordination number of Te is rather close to 4, in contrast to previous modelling results suggesting a Te coordination number in the range 3.6 to 3.7[29,30].

While instructive, the above analysis is still dependent on the choice of the cutoff distances. One way to go beyond this limitation lies in the use of MLWF formalism to define chemical bonds and therefore provide a direct count of the Te-O bonds in the disordered system. A chemical bond is defined between two atoms α and β if they share a Wannier center that satisfies the following inequality: $|d_{\alpha\beta} - d_{\alpha W} - d_{\beta W}| \leq 0.05$ Å. Where d is a distance, α and β refer to Te or O atoms, and a 0.05 Å tolerance is considered to account for small deviations that occurs on the spatial localization of the W center. In Ref. [29] the authors suggested that the position of the electronic lone pair of Te, and in particular the angle formed between the lone pair direction and the Te-O bonds is also a key property to define the chemical bonds in TeO_2 systems. In our case this corresponds to the position of the W^{LP}_{Te} centers. Actually, by inspecting the structure of the TeO_2 system we identified some configurations in which the W^{LP}_{Te} is facing one O atom (see Fig. 5(b)). In an ideal disphenoidial unit, the W^{LP}_{Te} should point out in the opposite direction of the space occupied by the O atoms.

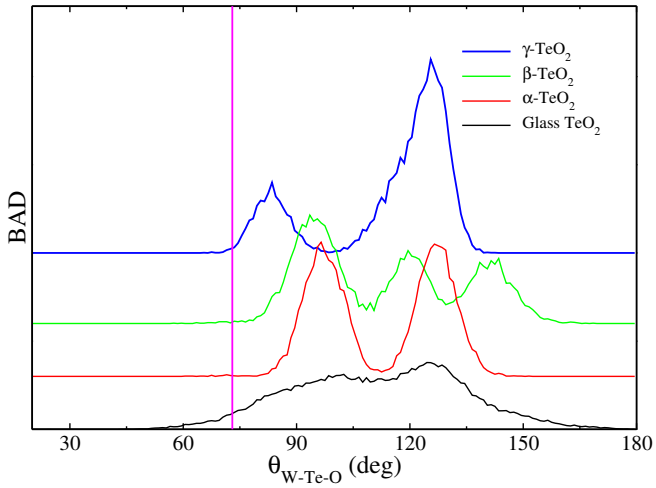

FIG. 7. Bond angle distribution $\theta_{W^{LP}_{Te}-Te-O}$ computed on α- (red lines), β- (green lines), γ-(blue lines), and amorphous (black lines) TeO_2 using a Te-O distance cutoff of 2.4 Å. The vertical line indicates the selected angle cutoff of 73°.

Hence, it appears necessary to define a cutoff angle between W^{LP}_{Te}, Te and O atoms to ignore lone pair Wannier centers that might occur at distances that satisfy the bonds inequality condition but do not correspond to bonds. To this end, we have calculated the W^{LP}_{Te}-Te-O bond angle distributions (BAD) in glassy as well as in the three crystalline phases of TeO_2. The crystals were annealed at T = 300K for 20 ps (PBE level of theory) and Wannier centers were calculated on top of 100 snapshots (PBE0 level of theory) extracted from the ambient temperature trajectory. Both functionals were first further tested by fully relaxing the structures of TeO_2 polymorphs, which showed lattice parameter changes within the range expected for DFT calculations (see Table S2 in the supplementary material[50]). The results for BAD are presented in Fig. 7.

The angular distribution of TeO_2 crystals features two main regions, the first in the 75-100° range, which corresponds to angles between the lone pair of Te and axial O atoms, and the second at 110-160° corresponding to contributions from equatorial oxygen atoms. As for the glassy TeO_2, we find

a broad peak at the region corresponding to typical features found in the crystals and a tail at angles below 73°. These results are in agreement with previous classical molecular dynamics results[29].

Following this analysis, a Te-O chemical bond is then defined upon the satisfaction of two conditions: (i) the bond inequality condition $|d_{\alpha\beta} - d_{\alpha W} - d_{\beta W}| \leq 0.05$ Å and (ii) the angular constraint $\theta_{W_{\mathrm{Te}}^{\mathrm{LP}}-\mathrm{Te}-\mathrm{O}} \geq 73°$. This procedure minimizes the impact of the choice of a fixed bond length cutoff and allows one to accurately estimate the coordination number of each chemical element by counting its number of chemical bonds. In addition, populations of l-fold coordinated Te and O can be also calculated.

Fig. 4 shows as dashed lines the n_{TeO} obtained with this procedure involving Wannier centers and angular constraints. The effects of varying $\theta_{W_{\mathrm{Te}}^{\mathrm{LP}}-\mathrm{Te}-\mathrm{O}}$ on n_{TeO} were found to be limited as shown in Fig. S4 in the supplementary material[50]. In marked contrast with previous methods, we find that the Te coordination numbers in both glassy and molten TeO_2 now reach a considerably stabilized (albeit yet slowly-evolving) plateau around a value of 4, and this remains true for Te-O bond lengths up to 3 Å. This result shows a very small dependency of the Te coordination number on the selected Te-O bond length (and here $\theta_{W_{\mathrm{Te}}^{\mathrm{LP}}-\mathrm{Te}-\mathrm{O}}$ angle) cutoff. By considering the cutoffs established based on the position of the Wannier centers, we find n_{TeO} of 3.96 and 3.65 in glassy and molten TeO_2, respectively. These numbers are smaller than those obtained by integrating the partial Te-O PDF and reflect the ability of the angular constraint condition to eliminate Te-O spatial proximities within the range of physical Te-O bonds but with electronic structure that are not consistent with the presence of a chemical bond. Our results are in very good agreement with the conclusions of Ref. [32] where n_{TeO} was found to be around 4 with a hint that it is smaller in the melt than in the glass.

Nevertheless, by inspecting the region of $r < 2.3$ Å in Fig. 4 one remarks that the experimentally measured n_{TeO} is larger in the melt than in the glass. The same trend is only visible in our models for distances below 1.97 Å. This behaviour is mainly due to the differences observed between the measured and the calculated $g_{TeO}(r)$ first peaks. Actually, the measured first peak corresponding to Te-O interactions is found to be more intense in the melt than in the glass, while the opposite is observed in our models. Generally, the intensity of $n_{TeO}(r)$ is subject to two competing effects: on the one hand, as the system is quenched the $g_{TeO}(r)$ first peak maximum is expected to increase due to the increasing number of short Te-O bonds in the glass, and on the other hand, when the system density increases the maximum of the peak is expected to decrease[64,65]. Hence, the small discrepancies between modelling and experiments might be due to the large error bar on the experimental density of the melt as well as the adopted quenching protocol[32].

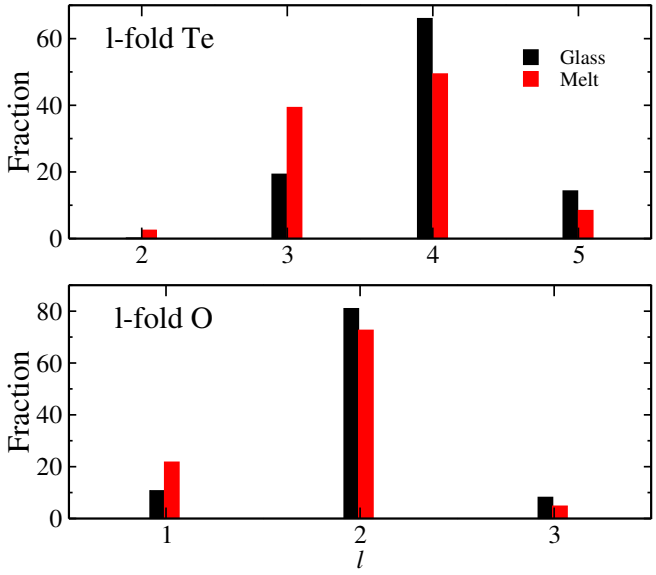

FIG. 8. Fractions of l-fold Te (l = 2, 3, 4 or 5) and O (l = 1, 2 or 3) computed on amorphous (black bars) and melt (red bars) TeO_2.

C. Atomic local environments and short range disorder

The coordination number reflects an average picture of the first coordination shell around a given atom. A more detailed picture can be obtained by decomposing the local environment into l-fold environments around Te and O, where l is the number of the nearest neighbors. These environments are determined using the same scheme as the coordination number and the corresponding results are shown in Fig. 8. Looking at Te atom in the glass, we find a dominant fraction (66.0 %) of TeO_4 units together with non negligible fractions of under-coordinated TeO_3 units (19.3 %) and over-coordinated TeO_5 units (14.3 %). We here neglect the fraction of 2-fold Te units as it is of the order of the statistical error ($\sim$ 2%). This distribution of Te local environment is in agreement with a Te average coordination number close to 4, as the under- and over-coordinated Te cancel out to promote an overall averaged 4-fold coordination sphere. This distribution undergoes a substantial modification in the melt where the fraction of TeO_4 and TeO_5 units reduces to 49.4% and 8.4%, respectively. This trend goes together with an increase of the population of TeO_3 motifs to reach 39.3 %. Taken all together, the evolution of the local environment of Te atoms is consistent with an elongation of some Te-O distances beyond the considered bonding threshold at high temperature in such that Te and O atoms are considerably far apart and consequently leads to a reduction of the average Te coordination number in the melt.

These findings are consolidated by looking at the analysis of the Q_m^n units (see table I). For every Te atom, m is its total coordination number and n represents the number of bridging O atoms (e.g. forming Te-O-Te bridges). Interestingly, we find a substantial increase in the fraction of Te units containing at least one non-bridging O atom (Q_3^1, Q_3^2 and Q_4^3) as a function of the temperature (see table I). Although indirectly,

TABLE I. Fractions of Q_m^n Te units found in glassy and melt TeO_2.

Q_m^n	Glass (%)	Liquid (%)
Q_3^1	-	2.5
Q_3^2	5.2	17.6
Q_3^3	14.1	19.2
Q_4^3	13.8	16.5
Q_4^4	52.0	32.1
Q_5^4	2.1	1.4
Q_5^5	12.2	6.9

one can infer that at high temperature the Te-O-Te bridges are subject to high thermal fluctuations that lead to a break down of weak Te-O bonds and consequently to a reduction of the Te coordination number. Furthermore, we remark that Te linkages with non-bridging O atom leads to distances significantly smaller that those occurring in Te-O-Te bridges, as shown in Fig. 9(b-d). This increase of the short range disorder around Te can be quantified by accessing the asymmetry of the Te-O bonds. To do so, we define for a given Te atom i the following average bond asymmetry function:

$$f_i = \frac{2}{m(m-1)} \sum_{j=1}^{m-1} \sum_{k=j+1}^{m} |d_{ij} - d_{ik}| \qquad (4)$$

where m is the number of O nearest neighbors of the Te atom i, and d the distance between the Te atom and one neighboring O. The average bond asymmetry f is thus zero for a Te atom having all its Te-O bonds lengths equal, and is positive when asymmetric bonds occur around Te. The same equation applies also for O centered bridges. Fig. 9(a-b) shows the distribution of f for various local environments of Te atom in the glassy and molten TeO_2. The distribution is normalized to the total number of Te atoms.

The total f distribution shows a broader spread in the melt than in the glass as well as a shift towards high f values indicating an increase of the bond asymmetry as the temperature increases. This evolution can be rationalized by looking at the break down of f as a function of the Te local environment, where we find that TeO_3 f distribution is largely shifted to higher values in the melt. Similar, but less important shift is also observed for the TeO_4 f distribution and goes together with a substantial broadening. These elements suggest that the increase of the disorder in TeO_4 units as the temperature increases, leads to a break of long and weak Te-O bonds, and consequently transforms into highly asymmetric TeO_3 units. These elements are inline with the hypothesis suggesting an increase of the short range disorder as a function of temperature leading to a reduction of the Te coordination number.

Coming to O atom, we find that it is mainly two-fold coordinated with a non-negligible fractions of one- and three-fold configurations. This result agree with a coordination number close to two for O atom. Interestingly, we find that the melt shows a larger fraction of 1-fold O atoms (21.8 %) compared to the glass (10.7 %). This increase of the fraction of 1-fold O as a function of temperature goes with a reduction of the

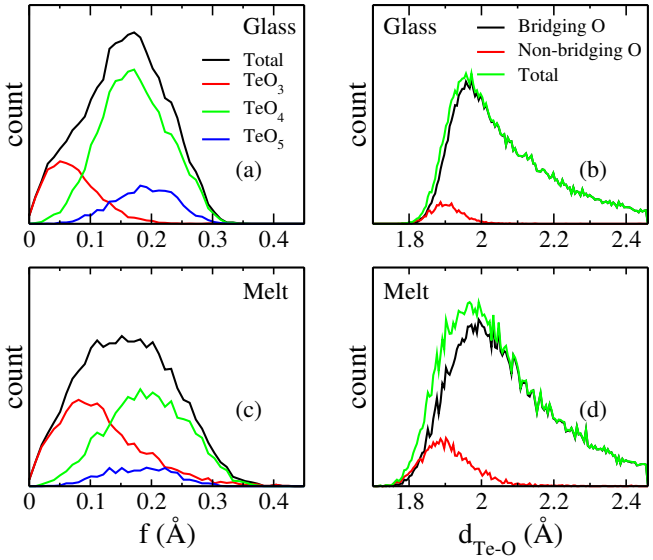

FIG. 9. Distribution of the average bond asymmetry function calculated on amorphous (a) and melt (c) TeO_2 and its breakdown into contributions from TeO_n units (n = 3, 4 and 5). Distribution of Te-O distances calculated on glass (b) and melt (d) TeO_2 where O atoms are either bridging or not bridging.

fractions of 2-fold (from 81.0 % in the glass to 72.6 % in the melt) and 3-fold (from 8.2 % in the glass to 4.8 % in the melt) O units. We note that the occurrence of 1-fold O atoms has to be correlated with the occurrence of terminal Te=O groups. This trend is in agreement with the increase of the fraction of under-coordinated Te atoms (TeO_3) and the increase of the Te environment asymmetry as a function of increasing temperature. Actually, our findings show that an average coordination number n_{TeO} less than 4 is not a straightforward proof of the occurrence of NBO in glassy TeO_2 as proposed previously, as the fractions of TeO_3 and TeO_5 motifs can be counterbalanced and lead to an overall n_{TeO} close to 4. These results are in agreement with the conclusions drawn based on NMR spectroscopy[31].

Fig. 10 shows the evolution of the distribution of Te-O bonds in Te-O-Te bridges as a function of the bridge asymmetry (denoted f) in glassy and molten TeO_2. For f values less than $\sim$ 0.2 Å Te-O distances show a broad distribution around the average Te-O bond length. Nevertheless, for larger values of f, we can clearly distinguish two populations of Te-O bonds one corresponding to short bonds of length less than $d_{TeO} = 2$ Å and another corresponding to long bonds with $d_{TeO} > 2$ Å. As f increases we find that the short bond exhibits a slow contraction while the long bond elongates rapidly. We remark that using f as a descriptor for the local environment asymmetry allows one to shed light into structural correlations that would not be observable otherwise. For example, no insightful information can be learned about the local environment by simply looking at the distribution of Te-O distances in Te-O-Te bridges as this leads to two broad and overlapping distributions. Coming to the melt, despite the broadening observed due to thermal fluctuations,

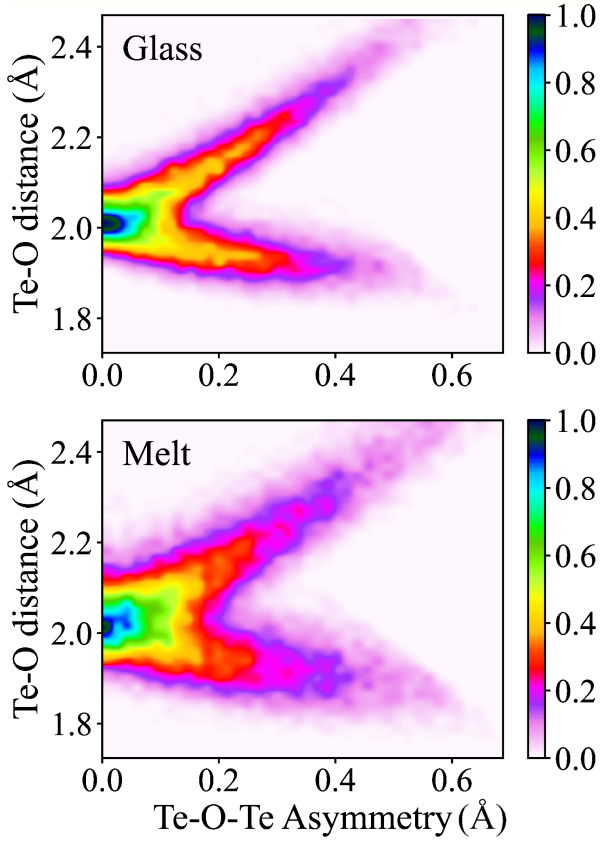

FIG. 10. Te-O distance vs the average bond asymmetry function is presented in glass (top) and melt (bottom) phases.

the same distance variations as a function of f hold true as in the case of the glass but with a slightly larger population of bridges with large asymmetry. These findings are perfectly in line with the distortion theorem of the bond-valence sum rule that states that in order to satisfy the valence of a given atom, when one of its bonds reduces, another bond has to undergo a larger elongation (leading to an increase of the average bond length)[66,67]. The above analysis supports the hypothesis that terminal Te=O groups can probably be formed due to the increasing asymmetry of the Te-O-Te bridges and particularly due to the elongation of one Te-O bond[32].

D. Atomic charge analysis and electron localization

We now correlate the Te and O local environments and coordination numbers to the electronic structure. To do so, we perform atomic charge analysis by resorting to the density derived electrostatic and chemical partitioning method (DDEC6)[68–71] as implemented in CHARGEMOL program[72]. In this charge partitioning scheme, the total electron density $\rho^{tot}(r)$ is partitioned into the atomic contributions $\rho_A(r)$ at each spatial position based on spherically symmetric weighting functions $w_A(r)$ built from reference ions:

$$\rho_A(r) = \rho^{tot}(r)\frac{w_A(r)}{\sum_i w_i(r)} \tag{5}$$

Subsequently, the net atomic charges (NACs) (q_A) on atom A are computed by integrating the atomic contribution over the whole space as follows

$$q_A = Z_A - \int \rho_A(r)dr \tag{6}$$

where Z_A is the atomic number of atom A (nuclear charge). We calculate the total electron density at the PBE0 level of theory by running an electronic structure minimization. We note that as pseudopotentials are used in our calculations, the core electrons are replaced by effective core potentials that are added back to $\rho_A(r)$ prior to DDEC6 partitioning.

In practice, DDEC6 charge partitioning employs a distributed multipole expansion to formally reproduce electrostatic potentials outside the electron distribution by partitioning the total electron density at each point in space among atoms in such a way that exactly one electron distribution is assigned to each atom. We note that DDEC6 method is a basis set independent scheme as it only depends on the the total electron distribution. Hence, no empirical parameter is needed in this approach which provides us with an independent tool to assess the short range order in terms of electronic structure. This method has been proved to be able to reproduce transferable NACs following Pauling scale electronegativity trends and chemically consistent with the assigned atomic spin moments[68]. Fig. 11 shows the evolution of Te and O NAC as a function of the coordination number and their distributions in TeO_2 glass and melt.

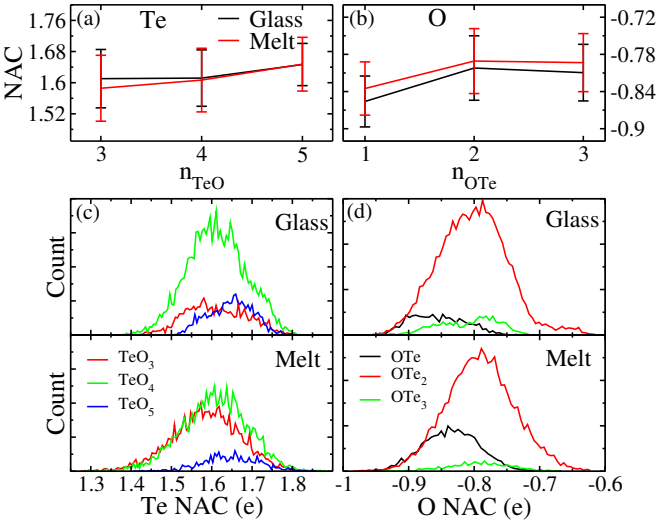

FIG. 11. Average net atomic charge (NAC) for l-fold Te (l=3,4,5) (a) and O (l=1,2,3) (b). In the bottom joint figures, distribution of NACs in the case of glass and melt for Te (c) and O (d) is represented.

We find that Te and O carry an average net charge of +1.62 e and -0.81 e in the glassy phase, respectively, in agreement

with the expected formal oxidation states ratio of these elements in TeO_2. Interestingly, Te shows a slightly lower NAC in the melt (+1.60 e) while the opposite occurs for O atoms (-0.80 e). The evolution of Te NAC as a function of n_{TeO} shows a slightly increasing trend in both glassy and molten TeO_2 reflecting that Te becomes more positively charged as more O atoms are added to its first coordination shell. This is particularly important for over-coordinated Te (5-fold Te) where their charge increase with respect to 4-fold Te by +0.04 e in the glass and +0.03 e in the melt. Looking at the O NAC evolution in figure 11(b), we find that 1-fold O shows a more negative NAC compare to 2-fold O with a reduction of -0.04 e and -0.05 e in the glass and melt, respectively.

In spite of their broadening and asymmetry, the distributions of net atomic charges computed for Te and O atoms show a clear correlation, in average, to the type of local structural environment (figure 11(c-d)). In the particular case of O, the strong change in the NAC of singly folded O atom might be attributed to the occurrence of Te=O chemical groups.

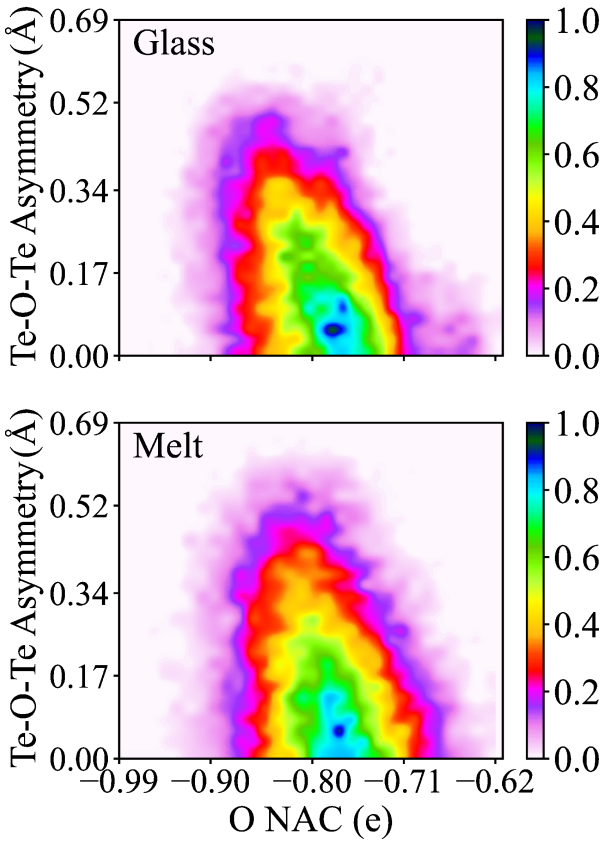

FIG. 12. For 2-fold oxygen, the distribution of Te-O-Te average bond asymmetry function (f) vs. the net atomic charge (NAC) is illustrated for glass and melt phases.

In order to rationalize the short range disorder in the Te-O-Te bridges in terms of electronic structure, we present in Fig. 12 the evolution of Te-O-Te bond asymmetry as a function of the 2-fold O NAC. Interestingly, we find an overall tendency of the 2-fold O NAC to be less important as their corresponding bond asymmetry increases in glassy and molten TeO_2. Having in mind that the increase of bridge asymmetry is mainly due to the elongation of one Te-O bond (see Fig. 10) and that singly fold O atoms feature a larger NAC compared to 2-fold O (see Fig. 11), one can put forward the following extrapolation: in a Te-O-Te bridge, the elongation of one Te-O bond leads to an increase of the bridge asymmetry and to an increase of the O NAC, if a Te atom is far enough from the O atom, the associated long Te-O bond can be considered as broken so that the O atom now belongs to a Te=O group and features substantially larger NAC. We note that, although there is no direct proof of this mechanism, our analysis shows concordant elements that makes it plausible.

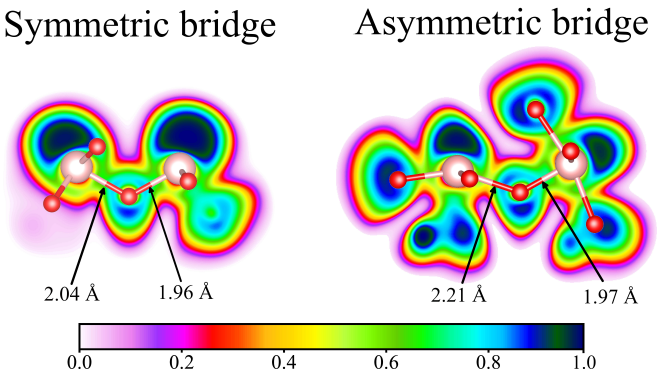

FIG. 13. Calculated ELF on the Te-O-Te plane of symmetric and asymmetric bridges in representative fragments of glassy TeO_2 network. The atomic structure of each fragment is superimposed on top of the ELF map. Only Te (brown color) and O (red color) above the Te-O-Te plane are shown. H atoms were used to make the O atoms passive and are not shown for clarity.

Another interesting marker of the bond asymmetry and electronic structure relationship is the electron localization function (ELF), as it correlates the free electron states (paired and unpaired electrons) to the nature of chemical bonds[73]. In practice, ELF is a spatial function with values ranging from 0 to 1. ELF values close to 1 suggest the occurrence of strong covalent interaction along a given bond, or lone pair electrons at the vicinity of a given atom, whereas lower ELF values represent weaker ionic, metallic, or van der Waals interactions. We here compute ELF on structural fragments extracted from the amorphous phase of TeO_2. Particularly, we select two structural motifs, one with a nearly symmetric Te-O-Te bridge (Te-O distances of 1.96 Å and 2.04 Å) and another with an asymmetric Te-O-Te bridge (Te-O bonds with 1.97 Å and 2.21 Å). For both motifs, we consider the complete coordination shells of Te atoms and passivate O with H atoms to ensure an overall charge neutrality. ELF is calculated at the PBE0 level of theory after relaxing H atoms at fixed Te and O positions. Figure 13 shows the obtained ELF results calculated in the plane containing the Te-O-Te bridge. For both symmetric and asymmetric bridges we remark a strong electron localization with ELF values larger than 0.7 at the vicinity of Te and O atoms which has to be correlated with

electron lone pairs of the considered atoms. Looking along the symmetric Te-O-Te bridge, we find a high electron localization on both sides of the central O atom with ELF values larger than 0.6 indicating that the electrons are almost equally shared between the two Te atoms and the central O atom. In addition, ELF distribution reduces as one approaches the Te atom reflecting therefore the iono-covalent nature of the Te-O bonds in this fragment. In the case of asymmetric Te-O-Te bridge one remarks that the electron localization distribution exhibits sizeable changes. In particular, while along the short Te-O bond one can observe similar ELF distribution to that observed around the symmetric bridge, along the long Te-O bond one observes an important reduction of ELF to values below 0.5 (see Fig. 13), suggesting thereby the occurrence of a weaker and more ionic Te-O bond. O atoms captures a higher fraction of shared electrons and consequently become more negative. These results confirm the DDEC6 charge analysis where a correlation between the bridge asymmetry and the O NAC has been observed.

IV. CONCLUSIONS

In summary, we have carried out first-principles molecular dynamics by resorting to a variety of DFT based schemes. The produced models allowed us to assess the effects of the choice of the DFT XC functional, model size effects, quenching rate and variable density effects on the final structure of TeO_2 glass. We find that the best agreement between the produced models and experimental data is achieved at the hybrid exchange and correlation functional level of theory combined with a variable density melt-quench approach. We note that the obtained TeO_2 atomic scale model can further be improved by considering statistical averages over multiple trajectories. Next, we concentrate our efforts on the calculation of the Te coordination number. We show that, although the integration of the partial PDFs allows us to reproduce the experimental measurements, it does not provide a straightforward value of n_{TeO} as a clear Te-O distance cutoff cannot be established. To cope with this limitation, we resort to the Wannier function formalism and provide a cut-off independent definition of the chemical bonds based on the positions of the Wannier centers and the geometry of the Te local environment. Based on this approach, we demonstrate that Te features a coordination number of 3.96 in the glass and 3.65 in the melt, in excellent agreement with recent experimental results. The study of the atomic local environments reveals that Te is mainly found in 4-fold units with a non-negligible fractions of 3- and 5-fold units, while O typically occurs in 2-fold units with a substantial fraction of non-bridging and 3-fold O atoms. The fraction of non-bridging O increases with the temperature which explains the observed reduction of the Te coordination number.

Furthermore, we focus on the short range disorder around Te and O and show that the melt exhibits an overall broader distribution of asymmetry around both species. In the case of Te, we infer that the increase of the temperature leads to an increase of the TeO_4 units asymmetry (f) that transform it into a highly asymmetric TeO_3 units. As the asymmetry of two-fold O increases we observe that the short bond undergoes a slow contraction while the long bond elongates steadily which provides a plausible hypothesis of the transformation of Te-O-Te bridges into terminal Te=O groups due to the increase of the short range disorder around O atom.

The study of the net atomic charge shows that Te features a slightly lower charge in the melt while O features a slightly larger charge. Interestingly, we find that 5-fold Te and 1-fold O show more important NAC compared to other Te and O structural units, respectively. Moreover, our results highlight the correlation between the 2-fold O NAC and the Te-O-Te bridge asymmetry, where the O NAC tend to have larger negative values when f increases. The study of the electron localization function of a symmetric and an asymmetric Te-O-Te bridge shows that in the first case, Te-O bonds are iono-covalent with a substantial charge localization along the bond and a higher ELF values at the vicinity of O, while in the second case, the short bond shows a charge localization similar to that observed in symmetric bridge whereas the long bond shows a low charge localization along the Te-O connection which indicates an ionic character on this bond.

In summary, the picture stemming out of our work describes TeO_2 as a network made of a variety of TeO_n units featuring a substantial short range disorder. This disorder translates into bond asymmetry and increases as a function of the temperature. As a consequence, the coordination number of Te reduces from ~ 4 in the glass to 3.65 in the melt. In addition, the increasing disorder around two fold-O atoms leads to the elongation of one Te-O bond and subsequently to the increase of the O negative charge, which tends towards that observed for non-bridging O atoms. Hence, both structural and electronic properties analyses corroborate the occurrence of Te=O groups in TeO_2.

ACKNOWLEDGMENTS

This work was supported by the ANR via the TRAFIC project (ANR-18-CE08-0016-01) and by région Nouvelle Aquitaine via the F2MH project AAP NA 2019-1R1M01. Calculations were performed by using resources from Grand Equipement National de Calcul Intensif (GENCI, grants No. A0080910832, A0080910832, A0100910832 and A0120910832). We are grateful to TGCC for the generous cpu allocation within the special session project spe00019. We used computational resources provided by the computing facilities Mésocentre de Calcul Intensif Aquitain (MCIA) of the Université de Bordeaux and of the Université de Pau et des Pays de l'Adour.

* assil.bouzid@unilim.fr

[1] J. E. Stanworth, J. Soc. Glass Technol. **38**, 425 (1954).

[2] H. Brger, W. Vogel, and V. Kozhukharov, Infrared Phys. **25**, 395 (1985).
[3] M. Weber, J. Non-Cryst. Solids **123**, 208 (1990), xVth International Congress on Glass.
[4] E. Vogel, M. Weber, and D. Krol, Phys. Chem. Glas. **32**, 231 (1991), cited By 398.
[5] R. A. H. El-Mallawany, *Tellurite Glasses Handbook : Physical Properties and Data, Second Edition* (CRC Press, 2016).
[6] T. Honma, N. Ito, T. Komatsu, and V. Dimitrov, J. Am. Ceram. Soc. **93**, 3223, https://ceramics.onlinelibrary.wiley.com/doi/pdf/10.1111/j.1551-2916.2010.03852.x.
[7] H. Nasu, O. Matsushita, K. Kamiya, H. Kobayashi, and K. Kubodera, J. Non-Cryst. Solids **124**, 275 (1990).
[8] K. Kimura, Jpn. J. Appl. Phys. **28**, 810 (1989).
[9] S. Tanabe, K. Hirao, and N. Soga, J. Non-Cryst. Solids **122**, 79 (1990).
[10] M. Colas, P. Thomas, J.-C. Champarnaud-Mesjard, and E. Fargin, Physics and Chemistry of Glasses - European Journal of Glass Science and Technology Part B **44**, 349 (2003).
[11] S. Suehara, P. Thomas, A. P. Mirgorodsky, T. Merle-Méjean, J. C. Champarnaud-Mesjard, T. Aizawa, S. Hishita, S. Todoroki, T. Konishi, and S. Inoue, Phys. Rev. B **70**, 205121 (2004).
[12] A. P. Mirgorodsky, M. Soulis, P. Thomas, T. Merle-Méjean, and M. Smirnov, Phys. Rev. B **73**, 134206 (2006).
[13] M. Soulis, T. Merle-Mjean, A. Mirgorodsky, O. Masson, E. Orhan, P. Thomas, and M. Smirnov, J. Non-Cryst. Solids **354**, 199 (2008), physics of Non-Crystalline Solids 11.
[14] M. Smirnov, A. Mirgorodsky, O. Masson, and P. Thomas, J. Phys. Chem. A . **116**, 9361 (2012), pMID: 22928634, https://doi.org/10.1021/jp303014k.
[15] B. Stehlik and L. Balak, Chem. Papers **2**, 6 (1948).
[16] P. Thomas, J. Phys. C: Sol. State Phys. **21**, 4611 (1988).
[17] H. Beyer, Zeitschrift Für Kristallographie-Crystalline Materials **124**, 228 (1967).
[18] S. Blanchandin, P. Marchet, P. Thomas, J. Champarnaud-Mesjard, B. Frit, and A. Chagraoui, J. Mater. Sci. **34**, 4285 (1999).
[19] A. Gulenko, *PhD: Structural study of amorphous TeO_2 and disordered δ-TeO_2 phase by molecular dynamics simulations* (University of Limoges, 2014).
[20] E. M. Roginskii, V. G. Kuznetsov, M. B. Smirnov, O. Noguera, J.-R. Duclre, M. Colas, O. Masson, and P. Thomas, J. Phys. Chem. C **121**, 12365 (2017), https://doi.org/10.1021/acs.jpcc.7b01819.
[21] E. R. Barney, A. C. Hannon, D. Holland, N. Umesaki, M. Tatsumisago, R. G. Orman, and S. Feller, J. Phys. Chem. Lett. **4**, 2312 (2013), https://doi.org/10.1021/jz4010637.
[22] M. N. Garaga, U. Werner-Zwanziger, J. W. Zwanziger, A. DeCeanne, B. Hauke, K. Bozer, and S. Feller, J. Phys. Chem. C **121**, 28117 (2017), https://doi.org/10.1021/acs.jpcc.7b08978.
[23] S. Sakida, S. Hayakawa, and T. Yoko, J. Non-Cryst. Solids **243**, 1 (1999).
[24] S. Sakida, S. Hayakawa, and T. Yoko, J. Non-Cryst. Solids **243**, 13 (1999).
[25] J. W. Zwanziger, J. C. McLaughlin, and S. L. Tagg, Phys. Rev. B **56**, 5243 (1997).
[26] J. McLaughlin, S. Tagg, J. Zwanziger, D. Haeffner, and S. Shastri, J. Non-Cryst. Solids **274**, 1 (2000), physics of Non-Crystalline Solids 9.
[27] J. C. McLaughlin, S. L. Tagg, and J. W. Zwanziger, J. Phys. Chem. B **105**, 67 (2001).
[28] U. Hoppe, I. Gugov, H. Brger, P. Jóvári, and A. C. Hannon, J. Phys. Condens. Matter **17**, 2365 (2005).
[29] A. Gulenko, O. Masson, A. Berghout, D. Hamani, and P. Thomas, Phys. Chem. Chem. Phys. **16**, 14150 (2014).
[30] F. Pietrucci, S. Caravati, and M. Bernasconi, Phys. Rev. B **78**, 064203 (2008).
[31] M. A. Marple, M. Jesuit, I. Hung, Z. Gan, S. Feller, and S. Sen, J. Non-Cryst. Solids **513**, 183 (2019).
[32] O. Alderman, C. J. Benmore, S. Feller, E. Kamitsos, E. Simandiras, D. G. Liakos, M. Jesuit, M. Boyd, M. Packard, and R. Weber, J. Phys. Chem. Lett. **11**, 427 (2019).
[33] H. Matsumoto, T. Mabuchi, Y. Shigesato, and I. Yasui, Jpn. J. Appl. Phys. **35**, 694 (1996).
[34] L. Torzuoli, A. Bouzid, P. Thomas, and O. Masson, Mater. Res. Express **7**, 015202 (2020).
[35] J. P. Perdew, K. Burke, and M. Ernzerhof, Phys. Rev. Lett **77**, 3865 (1996), *erratum* Phys. Rev. Lett. **78**, 1396 (1997).
[36] A. D. Becke, Phys. Rev. A **38**, 3098 (1988).
[37] C. Lee, W. Yang, and R. G. Parr, Phys. Rev. B **37**, 785 (1988).
[38] N. Troullier and J. L. Martins, Phys. Rev. B **43**, 8861 (1991).
[39] R. Car and M. Parrinello, Phys. Rev. Lett. **55**, 2471 (1985).
[40] J. Hutter, M. Parrinello, D. Marx, P. Focher, M. Tuckerman, W. Andreoni, A. Curioni, E. Fois, U. Röthlisberger, P. Giannozzi, *et al.*, IBM Zurich Research Laboratory and MPI für Festkörperforschung **2001** (1995).
[41] S. Nosé, J. Chem. Phys. **81**, 511 (1984).
[42] S. Nosé, Mol. Phys. **52**, 255 (1984).
[43] W. G. Hoover, Phys. Rev. A. **31**, 1695 (1985).
[44] J. VandeVondele, M. Krack, F. Mohamed, M. Parrinello, T. Chassaing, and J. Hutter, Comput. Phys. Commun. **167**, 103 (2005).
[45] J. VandeVondele and J. Hutter, J. Chem. Phys. **127**, 114105 (2007).
[46] S. Goedecker, M. Teter, and J. Hutter, Phys. Rev. B **54**, 1703 (1996).
[47] J. P. Perdew, M. Ernzerhof, and K. Burke, J. Chem. Phys. **105**, 9982 (1996).
[48] C. Adamo and V. Barone, J. Chem. Phys. **110**, 6158 (1999).
[49] T. D. Kühne, M. Krack, F. R. Mohamed, and M. Parrinello, Phys. Rev. Lett. **98**, 066401 (2007).
[50] Supplemental Material, "See supplemental material for details about teo_2 glass and melt modelling at the gga levelof theory, size and thermal effects, wannier function spread, details of the crystalline polymorphs and teo coordination number." `https://URLwillbeinsertedbypublisher`.
[51] A. Bouzid, C. Massobrio, M. Boero, G. Ori, K. Sykina, and E. Furet, Phys. Rev. B **92**, 134208 (2015).
[52] M. Ceriotti, F. Pietrucci, and M. Bernasconi, Phys. Rev. B **73**, 104304 (2006).
[53] O. Masson and P. Thomas, J. Appl. Crystallogr **46**, 461 (2013).
[54] T.-J. Chen and C.-L. Kuo, J. Appl. Phys. **110**, 064105 (2011).
[55] J. Huang, F. Lin, and C. Hin, Appl. Surf. Sci. **483**, 616 (2019).
[56] E. Tea, J. Huang, and C. Hin, J. Phys. D: Appl. Phys. **49**, 095304 (2016).
[57] M. Kaviani, J. Strand, V. V. Afanas' Ev, and A. L. Shluger, Phys. Rev. B **94**, 020103 (2016).
[58] P. Broqvist and A. Pasquarello, Microelectronic engineering **84**, 2022 (2007).
[59] M. Ceriotti, F. Pietrucci, and M. Bernasconi, Phys. Rev. B **73**, 104304 (2006).
[60] A. Kalampounias, G. Tsilomelekis, and S. Boghosian, J. Chem. Phys. **142**, 154503 (2015).
[61] J. Joannopoulos and M. L. Cohen, in *Sol. Sta. Phys.*, Vol. 31 (Elsevier, 1976) pp. 71–148.
[62] R. Resta and S. Sorella, Phys. Rev. Lett. **82**, 370 (1999).
[63] N. Marzari and D. Vanderbilt, Phys. Rev. B **56**, 12847 (1997).
[64] K. Wezka, A. Bouzid, K. J. Pizzey, P. S. Salmon, A. Zeidler, S. Klotz, H. E. Fischer, C. L. Bull, M. G. Tucker, M. Boero, S. Le Roux, C. Tugne, and C. Massobrio, Phys. Rev. B **90**,

054206 (2014).
[65] A. Bouzid, K. J. Pizzey, A. Zeidler, G. Ori, M. Boero, C. Massobrio, S. Klotz, H. E. Fischer, C. L. Bull, and P. S. Salmon, Phys. Rev. B **93**, 014202 (2016).
[66] I. D. Brown, *The chemical bond in inorganic chemistry: the bond valence model*, Vol. 27 (Oxford University Press, 2016).
[67] R. Allmann, Monatshefte für Chemie/Chemical Monthly **106**, 779 (1975).
[68] T. A. Manz and N. G. Limas, RSC Adv. **6**, 47771 (2016).
[69] N. G. Limas and T. A. Manz, RSC Adv. **6**, 45727 (2016).
[70] T. A. Manz, RSC Adv. **7**, 45552 (2017).
[71] N. G. Limas and T. A. Manz, RSC Adv. **8**, 2678 (2018).
[72] Chargemol, "Program computing ddec atomic charges," `https://sourceforge.net/projects/ddec/` (2017), accessed: 2022-01-10.
[73] M. Kohout, Int. J Quan. Chem. **97**, 651 (2004).

Supplementary Material: The structure of amorphous TeO_2 revisited: A hybrid functional *ab-initio* molecular dynamics study

Raghvender Raghvender, Assil Bouzid, Sylvian Cadars, David Hamani, Philippe Thomas and Olivier Masson

TEO_2 MELT AND GLASS MODELLING

Seven models with varying DFT setups (see Tab. S1) were produced as follows: **Model S1**, hereafter termed as CPMD-PBE-270, is made out of 270 atoms (90 Te and 180 O) in a periodic cubic box of 16.23 Å side length corresponding to the experimental density[4] of 5.57 g cm^{-3}. Starting from a random initial configuration, the system followed a melt-quench thermal cycle using the CPMD method as follows: 5 ps at T = 300K, 5 ps at T = 600K, 45 ps at T = 1000K, 30ps at T = 600K and 30 ps at T = 300K. Both Te and O showed a significant diffusion at the melting temperature of 1000 K thereby ensuring a complete decorrelation from the initial random configuration. **Model S2**, hereafter termed as CPMD-BLYP-270, was produced adopting a similar setup as in the case of Model S1 except the use of the BLYP XC functional. **Model S3**, hereafter termed as CPMD-BLYP-480, is a 480 atoms model (160 Te and 320 O) at the experimental density. The glass phase was produced using CPMD and BLYP XC functional after a thermal cycle as follows: 9 ps at T = 300K, 8 ps at T = 600K, 30 ps at T = 1000K, 25ps at T = 600K and 20 ps at T = 300K. The starting point of **model S4**, hereafter termed as CP2K-BLYP-480, is the last configuration of Model 3 at 1000K that was annealed for a further 15 ps at the same temperature using CP2K and BLYP XC functional. The system was then quenched to produce the glass in two steps: 14 ps at T = 600K, and 10 ps at T = 300K. **Model S5**, hereafter termed as SGCPMD-PBE-270, was produced through the second generation Car-Parrinello molecular dynamics and PBE XC functional on a 270 atoms system at the experimental density. A long quenching protocol was adopted for this model and features 370 ps detailed as followed: 45 ps for T = 1000K, 45 ps for T = 900K, 45 ps for T = 800K, 45 ps for T = 700K, 45 ps for T = 600K, 45 ps for T = 500K, 50 ps for T = 400K, and 50 ps for T = 300K (see Tab. S1). **Model 1 (see paper)**, hereafter termed as CP2K-PBE0-270, was produced by resorting to Born-Oppenheimer MD using the CP2K code and the hybrid PBE0 XC functional. Starting from the last obtained configuration of Model S1 at T = 300K, a thermal annealing cycle was applied to the system as follows: 1 ps at T = 300K, 3 ps at T = 900K, 4 ps at 1200K, 3 ps at T = 900K, 3 ps at T = 600K, and 5 ps at T = 300K. We note that, given the very high cost of hybrid functional molecular dynamics, we anneal the system at T = 1200K, a temperature slightly higher than the melting point (T = 1006K) in order to induce significant rearrangement of the structure and adapt to the used DFT setup. Finally, **Model 2 (see paper)**, CP2K-PBE0-variable-density-270, was produced by melt quenching using CP2K and PBE0 XC functional and allowing the density of the system to increase linearly from 5.09 gcm^{-3} at the melt state[1] to 5.57 gcm^{-3} at ambient temperature[4]. Precisely, the system was subject to the following variable density thermal cycle: 5 ps at T = 1200K and ρ=5.09 g cm^{-1}, 5 ps at T = 1000K and ρ=5.09 g cm^{-3}, 5 ps at T = 750K and ρ=5.25 g cm^{-3}, 5 ps at T = 500K and ρ=5.40 gcm^{-3}, and 6 ps at T = 300K and ρ=5.57 g cm^{-3}. For all the models, statistical averages are performed on at least a 5 ps trajectory.

Model	Ab-Initio code	Pseudo-potential	Number of atoms	Heat-Quench cycle (Temperature)	Description
Model S1	CPMD	PBE	270	5ps (300K), 5ps (600K), 45ps (1000K), 30ps (600K), 30ps (300K)	At experimental constant density of 5.57 g/cm^3. Started from random initial configuration.
Model S2	CPMD	BLYP	270	5ps (300K), 5ps (600K), 45ps (1000K), 30ps (600K), 30ps (300K)	At experimental constant density of 5.57 g/cm^3. Started from random initial configuration.
Model S3	CPMD	BLYP	480	9ps (600K), 8ps (600K), 30ps (1000K), 25ps (600K), 20ps (300K)	At experimental constant density of 5.57 g/cm^3. Started from random initial configuration.
Model S4	CP2K	BLYP	480	— — 15ps (1000K), 14ps (600K), 10ps (300K)	At experimental constant density of 5.57 g/cm^3. Started from last configuration of Model S3 at 1000K.
Model S5	SGPCMD	PBE	270	45ps (1000K), 45ps (900K), 45ps (800K), 45ps (700K), 45ps (600K), 45ps (500K), 50ps (400K), 50ps (300K)	At experimental constant density of 5.57 g/cm^3. Started from last configuration of Model S4 at 300K.
Model 1	CP2K	PBE0	270	1ps (300K), 3ps (900K), 4ps (1200K), 3ps (900K), 3ps (600K), 5ps (300K)	At experimental constant density of 5.57 g/cm^3. Started from last configuration of Model S1 at 300K.
Model 2 (Variable density)	CP2K	PBE0	270	5ps (1200K) @ 5.09 g/cm^3, 5ps (1000K) @ 5.09 g/cm^3, 5ps (750K) @ 5.25 g/cm^3, 5ps (500K) @ 5.40 g/cm^3, 6ps (300K) @ 5.57 g/cm^3	With variable density. Started from last configuration from Model 1 at 1200K

TABLE S1. Various DFT setups used to study the model best capable of describing experimental data. In addition, the thermal cycle used for heat and quench is also reported.

GGA FUNCTIONAL EFFECTS

The choice of the DFT XC functional can have an impact on the structure of the glassy phase as well as on its properties[3]. In this work, we investigate the effects of the XC functional on tellurium oxide by focusing on model S1 (CPMD-PBE-270) and model S2 (CPMD-BLYP-270) which were generated following an identical protocol except the use of PBE XC functional in Model S1 and BLYP XC functional in Model S2. Figure S1 reports the calculated total pair distribution functions in the molten and glassy states of TeO_2 compared to experimental measurements. We remark that both models show a first peak position slightly shifted towards large distances by about 0.06 Å as compared to experiments. In addition, the shapes of the second and third peaks located between 3 Å and 5.5 Å obtained with both PBE and BLYP functionals lead to a very similar results within typical statistical fluctuations. Such results are consistent with previous work on crystalline phases of TeO_2 where PBE and BLYP led to very similar results in terms of local structure.[5] Nevertheless, both functionals fail to reproduce the experimental PDFs of the molten and glassy TeO_2. In particular, this failure is visible at two levels: experimentally the second peak located at around 3.7 Å in the melt is found to move towards 3.55 Å in the glass, and the intensity of the third peak located around 4.3

Å increases when going from the melt to the glass. While, PBE and BLYP models show the same shape of the second peak calculated for the melt and glassy TeO_2, they fail in reproducing the third PDF peak measured experimentally. As such, one might conclude that computational setups of Models S1 and S2 are insufficient to achieve a quantitative description of the TeO_2 systems.

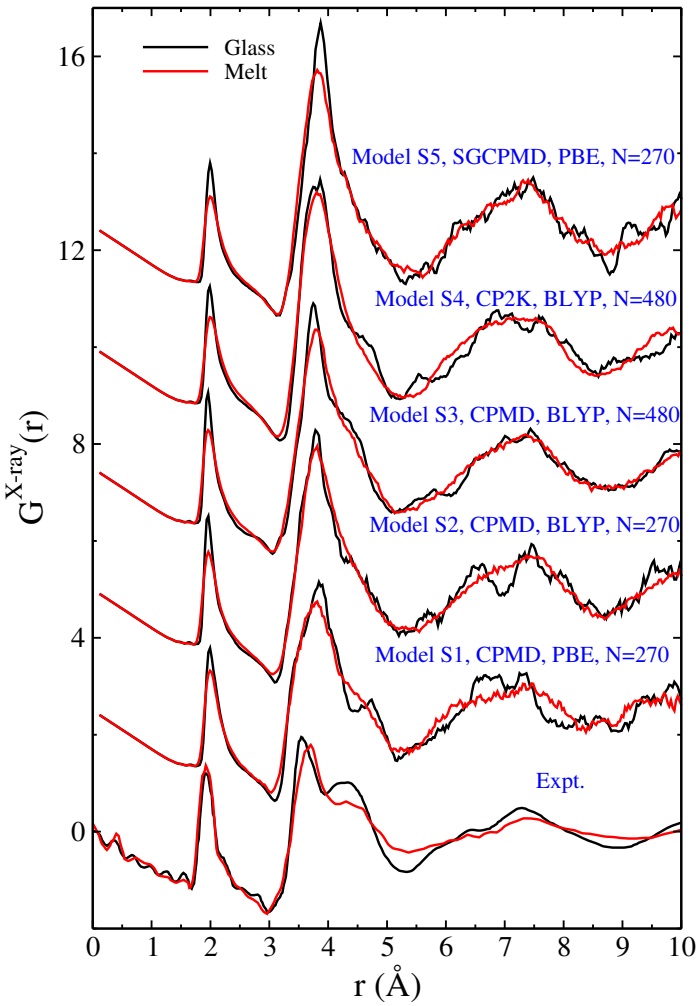

FIG. S1. Total X-ray PDF computed for amorphous (black lines) and melt (red lines) TeO_2 obtained from Models (from bottom to top) 1, 2, 3, 4 and 5 and compared to experimental results from Ref. [1]. The curves are shifted vertically for clarity.

SIZE EFFECTS

One possible issue that can affect FPMD disordered models is related to the adopted size of the model. In fact, using small periodic models might lead to an ill description of the glassy network, particularly when the system features extended structural motifs such as rings, chains or voids. In the case of TeO_2, we assess this issue by producing two models with 480 atoms: CPMD-BLYP-480 and CP2K-BLYP-480. The calculated PDFs of both models are presented in Figure S1. Despite the use of different molecular dynamics schemes (CPMD and BOMD), we find very similar PDFs for the molten and glassy TeO_2 with 480 atoms. In particular, for r values less than 5 Å one cannot distinguish any sizeable differences in the overall shape of the PDF from the 270 and 480 atoms models. As for distances beyond 5 Å, the small observed fluctuations are typical of statistical fluctuations in the glass. These results suggest that beyond 270 atoms the model sizes have a limited influence on the description of the short to medium-range structure of TeO_2. Worth to note, these models (CPMD-BLYP-270, CPMD-BLYP-480 and CP2K-BLYP-480) were produced independently from different initial states, in otherwise similar conditions, turn out to have highly similar structures, which underlines the statistical stability of our modeling strategy.

THERMAL CYCLE EFFECTS

The quenching rate is another parameter in FPMD modelling that can alter the structure of the glass. Despite the fact that FPMD cannot reach realistic quenching rates, we investigate here the effects of the quenching cycles by comparing the final structures obtained from Model S1 (CPMD-PBE-270) where the quench is performed in two steps at T = 600 K and T = 300 K, and Model S5 (SGCPMD-PBE-270) where the temperature is reduced by steps of 100 K with an annealing of 45ps at each temperature. The corresponding computed PDFs are shown in figure in Figure S1. We find that both thermal cycles lead to very similar PDFs indicating a limited effect of the quenching rate on the final structure of the glass. In addition, the PDFs do not reflect the differences between the molten and the glassy states measured experimentally. We note that, one cannot rule out that a very slow quenching rate, orders of magnitude larger than the one used in this study, can lead to relaxations of the glassy structure.

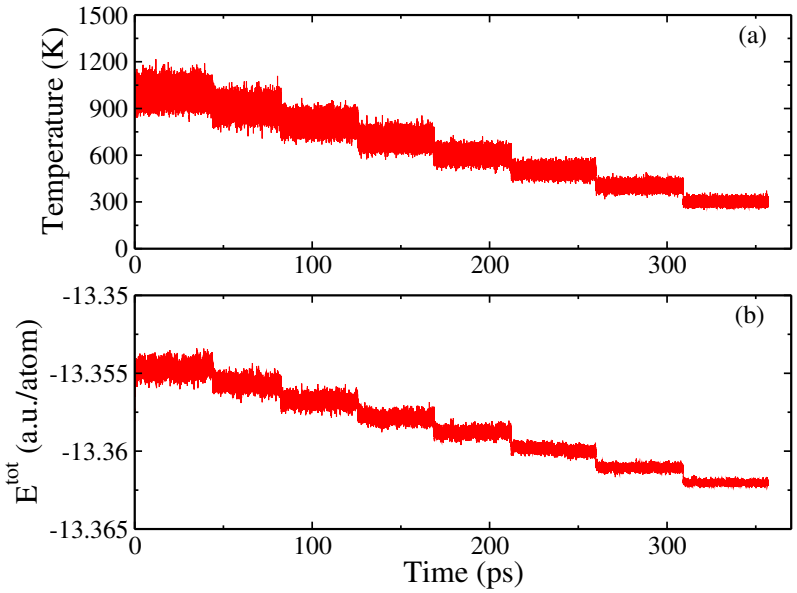

FIG. S2. Temperature (a) and total energy (b) evolution during the quenching cycle of Model 5.

WANNIER FUNCTION SPREAD

We focus on what makes PBE0 better in describing the structure of TeO_2. Fig. S3 shows the distribution of the Wannier functions spread as a function of their distance from Te atom calculated at PBE0 (model 2) and PBE (model S1) level of theory. Regardless of the type of the Wannier center (W^{LP} or W^{B}), we remark that the absolute values of their spread is smaller in the case of PBE0 than PBE. This implies a better electronic localization from hybrid functional as expected.

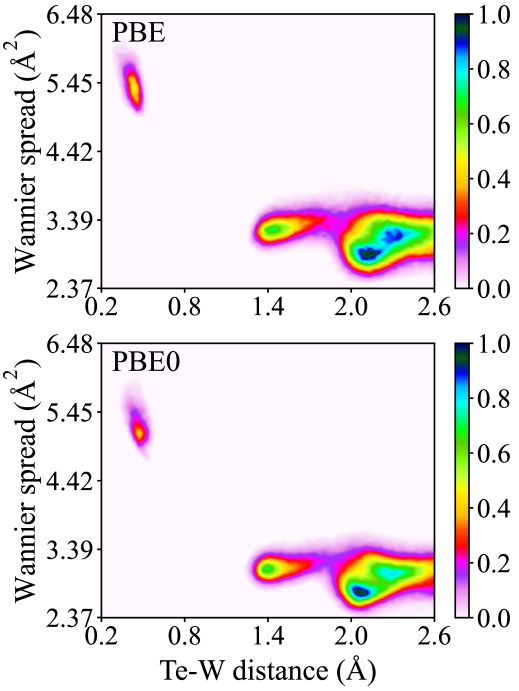

FIG. S3. The distribution of the Wannier functions spread as a function of the distance between Te atoms and the Wannier centers computed at the PBE level of theory (top panel) and PBE0 level of theory (bottom panel).

CRYSTALLINE POLYMORPHS

Crystal polymorphs	Experimental Lattice Parameter (Å)	PBE Lattice Parameter (Å) (% change)	PBE0 Lattice Parameter (Å) (% change)
α-TeO_2	A = 9.592	9.953 (3.76%)	9.761 (1.76%)
	B = 9.592	9.953 (3.76%)	9.761 (1.76%)
	C = 15.252	15.016 (1.55%)	15.070 (1.19%)
β-TeO_2	A = 24.07	23.293 (3.23%)	24.241 (0.71%)
	B = 10.928	11.059 (1.2%)	10.575 (3.23%)
	C = 11.214	11.714 (4.46%)	11.530 (2.82%)
γ-TeO_2	A = 9.796	10.644 (8.66%)	10.111 (3.22%)
	B = 17.152	16.663 (2.85%)	17.073 (0.46%)
	C = 8.702	8.451 (2.88%)	8.545 (1.8%)

TABLE S2. Description of lattice parameter change under structural relaxation of 2x2x2 unit cell in $\alpha-$, $\beta-$ and $\gamma-$ TeO_2 polymorphs using PBE and PBE0 functionals

TE-O COORDINATION NUMBER

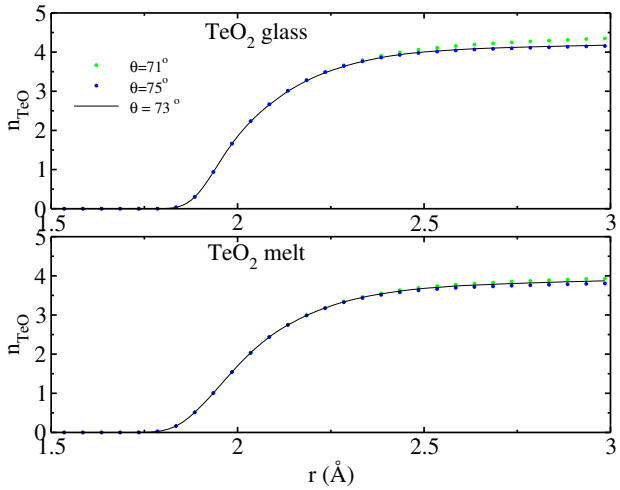

FIG. S4. Running Te-O coordination number ($n_{\mathrm{TeO}}(r)$) of amorphous (top panel) and melt (bottom panel) TeO_2. Results obtained based on Wannier centers with variable angular constraint thresholds.

[1] O. Alderman, C. J. Benmore, S. Feller, E. Kamitsos, E. Simandiras, D. G. Liakos, M. Jesuit, M. Boyd, M. Packard, and R. Weber, J. Phys. Chem. Lett. **11**, 427 (2019).
[2] O. Masson and P. Thomas, J. Appl. Crystallogr **46**, 461 (2013).
[3] A. Bouzid, C. Massobrio, M. Boero, G. Ori, K. Sykina, and E. Furet, Phys. Rev. B **92**, 134208 (2015).
[4] A. Gulenko, O. Masson, A. Berghout, D. Hamani, and P. Thomas, Phys. Chem. Chem. Phys. **16**, 14150 (2014).
[5] M. Ceriotti, F. Pietrucci, and M. Bernasconi, Phys. Rev. B **73**, 104304 (2006).